Relevance of C/O ratios in the gas-phase synthesis of freestanding few-layer graphene

Paolo Fortugno [a,*], Claudia-Francisca López-Cámara [a,b], Fabian Hagen [c], Hartmut Wiggers [a,b], Christof Schulz [a,b]

[a] *EMPI, Institute for Energy and Materials Processes – Reactive Fluids, University of Duisburg-Essen, Duisburg, Germany*
[b] *CENIDE, Center for Nanointegration Duisburg-Essen, University of Duisburg-Essen, Duisburg, Germany*
[c] *Engler-Bunte- Institute, Division of Combustion Technology, and Institute for Chemical Technology and Polymer Chemistry, Karlsruhe Institute of Technology (KIT), Karlsruhe, Germany*

ARTICLE INFO

ABSTRACT

In microwave-plasma synthesis of few-layer graphene from hydrocarbon precursors, the carbon-to-oxygen and the carbon-to-hydrogen ratios are known to influence the product ratio of graphene to amorphous soot-like particles. While the role of oxygenated hydrocarbons and water as oxygen-supplying species has been studied before, in this paper, we compare the effect of carbon dioxide, molecular oxygen, and nitrous oxide mixed with ethylene to systematically change the C/O ratio while keeping the hydrogen supply constant. *Ex situ* powder analysis, emission spectroscopy, gas chromatography, and simple reaction kinetics simulations are employed to evaluate and describe the synthesis process. Additionally, thermophoretically sampled nanomaterials are collected close after the first particle inception and analyzed *ex situ*. The results show that molecular oxygen and nitrous oxide increase the graphene fraction with decreasing C/O ratios and pure graphene is reached at 2:1.5. The decrease in C/O ratio results in an overall decrease in solid carbon yield. With carbon dioxide, pure graphene cannot be generated at a C/O ration of 2:1.5, although a similar reduction of the particle yield is observed. Thermophoretic sampling showed that the specific mixture of carbon allotropes is already defined a few cm downstream to the plasma zone. Emission spectroscopy shows that carbon dioxide forms carbon species during its decomposition in the plasma, we hypothesize that these released carbon species might influence the environment for local nucleation of solid carbon. Thus, the C/O ratio and *available* carbon fraction for growth cannot always be used to tailor the carbon microstructure. Moreover, the source of oxygen atoms also seems to have an effect on the resultant microstructure.

1. Introduction

Graphene has attracted considerable interest due to its unique properties such as high electrical and thermal conductivities, optical transparency, and mechanical strength [1]. A wide range of applications has been envisioned, from sensors [2–4] to optoelectronics [5,6], and transparent conductive films for solar cells [7]. In recent years, potential applications have been extended to catalysis [8,9], battery electrode materials [10,11], and supercapacitors [12,13], where graphene often serves as a flexible, conductivity-enhancing and electrochemically-stable component. Graphene is also of interest as additive for enhancing the mechanical, electrical, and thermal properties of polymer composites [14–16].

One way of continuously generating high-purity few-layer-graphene (FLG) flakes is the synthesis via atmospheric-pressure plasma pyrolysis of hydrocarbon reactants. In this method, the hydrocarbon reactant is passed through a plasma zone, which decomposes it into atomic species due to the high temperatures (>3000 K). Downstream, the gas temperature decreases leading to the formation of carbon containing gaseous species that can then nucleate into solid carbon allotropes. This method is also considered for reforming hydrocarbons towards hydrogen while harvesting solid carbon materials [17,18]. The mechanistic understanding required for directing particle formation and growth towards specific valuable allotropes is, however, still lacking.

In the past, multiple authors were able to show that tailoring specific experimental parameters e.g., reactant concentration, input power, and

---

pressure [19–23], can influence the type and quality of carbon allotrope grown during the plasma synthesis. The carbon-to-oxygen ratio (C/O ratio) in the hydrocarbon precursor was identified as one of the factors controlling the free-standing carbon-allotrope type formed in a plasma reactor [24,25]. Previous results showed that this C/O ratio can be interpreted as an artificial control of the carbon-atom concentration available for growth considering the formation of carbon monoxide (CO) as a loss channel. It was shown that water can also act as an oxygen source yielding graphene from oxygen-free hydrocarbons [26]. Yet, other results suggest that only focusing on oxygen as species reducing C through CO formation modifying the available carbon concentration is an oversimplification. The formation of particles was observed even when high concentrations of oxygen-containing species (e.g., CO_2 [27, 28]) or when ethyl acetate – in comparison to butyric acid and ethanol – with the "correct" C/O ratio and concentration [29] is supplied.

Independently, it was additionally shown in thermal [30–32] and microwave plasmas [33–35] that also the hydrogen concentration can be tailored for directing carbon inception and growth towards graphene. It is argued that hydrogen can saturate the surface of the growing clusters and thus suppress out-of-plane growth.

In this work, we investigate, whether the oxygen-atom source species has an impact on the graphene synthesis. For this purpose, we employ three different compounds (carbon dioxide, CO_2; nitrous oxide, N_2O; and molecular oxygen, O_2) that deliver oxygen atoms at plasma temperature at various C/O ratios while keeping the supply of hydrogen fixed. To this end, we combine *in situ* optical spectroscopy, inline gas analysis with thermophoretic sampling and *ex situ* materials characterization. The experimental findings are supported on the basis of simplified kinetics and chemical equilibrium simulations of the reaction system.

2. Experiment

The experimental setup consisted of the microwave-plasma reactor system shown in Fig. 1. A more detailed explanation can be found in previous works [26]. A quartz tube with inner diameter of 70 mm was positioned at the center of a cylindrical microwave slot antenna (Cyrannus, iplas GmbH). Radiation from a microwave generator (Muegge GmbH MH 20,005–213BA, 2.45 GHz, and maximum power 2 kW) was focused along the center of the fused-silica tube to generate a

standing wave that ignited and supported the plasma. The reactant mixtures (ethylene and oxygen carriers) were fed from the bottom into the plasma zone via a combination of two nozzles. A central nozzle provides the reactive gas mixture diluted in argon (Ar, 5.0 purity). The resulting gas flow was stabilized by a tangentially injected sheath gas flow of 30 slm Ar (5.0) and 1 slm hydrogen (H_2, 5.0). All gas flows were controlled with calibrated Bronkhorst mass flow controllers. For all experiments, ethylene ($C_2H_4 \geq 99.9\%$) was mixed upstream with Ar and sent into the reactor through the central nozzle. Depending on the case of study, O_2 (4.8), CO_2 (4.5), or N_2O (5.0) were added to the central ethylene/argon mixture (see Table 1 for details).

Each experiment started by evacuating the reactor to ~2000 Pa. Subsequently, the plasma was ignited at the magnetron (output power of 600 W) in a pure Ar flow sheath gas. H_2 was then added to the system, and the pressure and microwave power were stepwise increased up to 10^5 Pa and 1400 W. The oxygen-containing reactant (i.e., the oxygen carrier with the respective flowrate) and ethylene (190 sscm: standard cubic centimeters per minute) were then introduced into the reactor. Each experiment lasted around 1 h, after which the reactor was flushed with Ar. For thermophoretic particle sampling in the post-plasma flow, particles were deposited on lacey-carbon coated TEM grids that were exposed to the plasma region (~15 cm height above nozzle; HAN) by a pneumatically-driven piston. The actuation of the pneumatic system exposing the TEM grid for about ~10 ms was repeated 20 times to ensure sufficient sample collection. More details on the thermophoretic sampling system can be found in Refs. [36–38]. The carbonaceous products were also harvested from a filter placed at the reactor off-gas for more extensive powder analysis. Details on the different studied

Table 1
Oxygen-carrier type and volumetric flow rates (slm). Sheath gas for all cases: 30 slm Ar (5.0) and 1 slm H_2 (5.0) (slm: standard liters per minute).

Case	Oxygen carrier	Flow rate / sccm	Ar flow rate / slm	C/O ratio
1	None	0	5	∞
2–4	Oxygen (O_2)	47.5–142.5	5−x	2:0.5–2:1.5
5–7	Nitrous oxide (N_2O)	95–285	5−x	2:0.5–2:1.5
8–9	Carbon dioxide (CO_2)	190–285	5−x	2:1–2:1.5
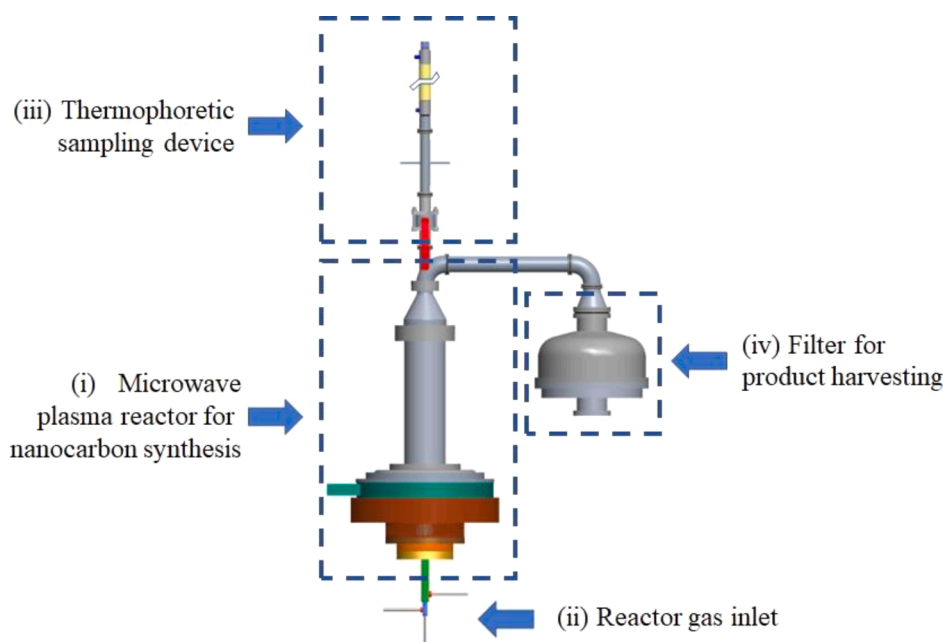
Fig. 1. Schematic of the microwave-plasma reactor including the thermophoretic sampling system and the filter used for particle collection.

cases are listed in Table 1.

Case 1 is established as the base case as it does not have any oxygen-carrier addition and solely ethylene (190 sccm) was used as reactant. From previous experiments, this case is known to produce a mixture of crumpled FLG, soot-like, and graphitic particles [26,35]. Thus, the flowrates were adopted from these previous studies. Cases 2–4, 5–7, and 8–9 were designed to investigate/screen the role of oxygen using different oxygen carriers (see C/O ratios from Table 1). To maintain a constant inlet gas flow for all experiments even with variable flows of oxygen carriers, the Ar flow was reduced respectively. The total flow rate was thus fixed at 5.19 slm (0.19 slm C_2H_4, x slm oxygen carrier, and (5 − x) slm Ar). The gas velocity of the reactive flow through the central nozzle is estimated to be ~6.8 m/s while the sheath gas flow is ~0.14 m/s (both values for $T = 0$ °C). Based on these inlet velocities, the Reynolds number for the reactive flow is ~2300 and for the sheath gas ~800. Using the approach of Lim and coworkers [39], this results in mixing times of 10–15 ms. It was assumed that at ~3700 K, one oxygen atom is released during the decomposition of N_2O and CO_2, and two for the case of O_2. The additional carbon and oxygen atom of CO_2 was neglected for the design of experiments and the calculation of C/O ratios. Thermophoretic sampling and gas chromatography coupled with mass spectrometry (GC/MS) measurements were performed for the cases with C/O ratios of 2:1.5 and the reference Case 1.

2.1. In situ temperature measurements from optical emission spectroscopy

Optical emission spectroscopy (OES) was used to obtain information about the plasma temperature and key species (details reported in Ref. [26]). Light emission of the plasma torch was collected with an open SMA optical fiber end connector (numerical aperture: 0.22, fiber core diameter: 0.6 mm) placed ~20 mm downstream of the microwave resonator, where the microwave shielding is installed, i.e., the light is collected through the holes of the microwave shield. The fiber position was adjusted for maximal Hα signal strength. The collected light was guided into a monochromator (SPEX 1704, 1200 g/mm grating, blazed for 400 nm) by two planoconvex fused silica lenses ($f_1 = 50$ mm, $f_2 = 150$ mm, diameter: 2.5 cm). The diffracted light was detected with a photomultiplier tube (Hamamatsu R955) with a spectral response between 160 and 900 nm, and recorded using LabVIEW. A Hg/Ar light source (LOT QuantumDesign) was employed for calibration. The spectral resolution of the OES system was about 0.02 nm (full-width-half-maximum; FWHM). The instrument function of the spectrometer system was corrected for using the known spectrum of a laser-driven light source (Energetiq LDLS EQ-99X) as reference.

2.2. Inline gas species diagnostics

GC/MS measurements were performed with an Agilent 7890A/ Agilent 5975C combination to probe the gas species concentrations downstream of the plasma (~0.8 m HAN). A Plot-Q column was used to separate the test-gas species. Samples were taken *in situ* during reactor operation by extracting gas samples into 3 l volume vacuum containers ($<10^{-3}$ mbar l s^{-1} leak rate) through a vacuum lock. Prior to sampling, the containers were purged and evacuated multiple times. Then, the containers were filled with the gaseous sample up to approx. 800 mbar (absolute pressure). Afterwards, the containers were transported and measured at the GC/MS system.

2.3. Ex situ materials characterization

The powders harvested from the filter were characterized for their microstructure, morphology, and chemical composition by transmission electron microscopy (TEM, Cs-corrected JEOL Jem 2200FS with 200 kV acceleration voltage), Raman spectroscopy (Renishaw inVia), thermogravimetric analysis (TGA), and X-ray photoelectron spectroscopy (XPS, PHI 5000 Versaprobe). The thermophoretically sampled particles

were analyzed by TEM only.

TEM and high-resolution TEM (HRTEM) samples (powders harvested from the filter) were prepared by dispersing a small amount of the sample powder in absolute ethanol (≥99.8% purity) followed by ultrasonication for 20 min. A few droplets of the dispersion were drop-casted on lacey copper TEM grids and dried under a fume hood. Contrary, the samples collected with the thermophoretic sampling system, were measured without further sample preparation as they were already on TEM grids.

For Raman spectroscopy, a small amount of sample powder was transferred onto a glass slide and compacted with a spatula. The measurements were done at room temperature and under ambient atmosphere, at wavenumbers between 300 and 3200 cm^{-1}. The device was operated with a 532 nm frequency-doubled continuous-wave Nd:YAG laser and a diffraction grating of 1800 l/mm. During measurement, the laser power was set to ~0.07 mW with a spot size of 10–15 μm in diameter. These conditions resulted in laser intensities of <100 W/cm^2, with negligible laser heating of the sample. Measurements were performed at least at two separate locations for each sample, because the carbon powder bed does not form a flat surface as required for recording Raman maps.

Thermogravimetric analysis was used to analyze the thermal oxidation rate of the samples with a Netzsch STA 4491 F1 Jupiter connected to a Netzsch QMS 403 D Aëolos for simultaneous mass spectroscopic measurements. For all these measurements, Ar-diluted artificial air (~15% O_2) was introduced into the sample chamber, in which materials were thermally treated from 40 to 1000 °C at a heating rate of 5 °C/min. The mass spectrometer was set up to monitor the mass-to-charge (m/z) ratios of water and CO_2 fragments in addition to artificial air and Ar.

For XPS analysis, powder samples were mounted on a double-sided 3 M Scotch tape onto the sample holder. Binding energies were measured at room temperature with a monochromatic Al-Kα source at $h\nu = 1486.6$ eV and at 45° between the specimen and the analyzer. All spectra were attained using 11.75 eV pass energy, and shifted relative using a 360 s etched Cu-foil surface as reference. The spectra were analyzed using the Casa XPS software.

3. Numerical simulation

Two different sets of simulations were performed. First, chemical equilibria of the gas mixture at the plasma temperature were calculated for reference Case 1 and for all added oxygen carriers with C/O ratios of 0 and 2:1.5 (Case 4, 7, and 9 before (i.e., C/O ratio = 0) and after C_2H_4 addition; C/O ratio = 2:1.5) for comparison with OES measurements. Secondly, kinetics simulations of the reactions occurring in the plasma region (from the nozzle exit and up to 0.5 m downstream) were performed to compare the resulting species concentration profiles from the simulation with the observed ones from OES and GC/MS measurements. The simulations were limited to the initial 0.5 m, because already at a distance of ~0.3 m from the plasma zone, temperatures below 1000 K were reached at which no further reactions were predicted. The main goal of the simulations was to qualitatively support the interpretation of the reaction environment leading to the observed solid materials by evaluating the concentrations of the gas species (CO, C_2H_2, C_2H_4) formed.

The simulations were performed with Ansys Chemkin-Pro 2023. Chemical equilibria were calculated with the chemical and phase equilibrium calculations module. Calculations were performed for 1 bar input pressure for the gas compositions described in the previous paragraph. A step size of 10 K in the range of 300–8000 K for constant temperature and volume was chosen. For the reaction kinetics simulations, the 1D plug-flow reactor module was chosen to mimic the experimental setup, because the module allows for fast and simple computation of the desired species profiles, while more elaborate 2D/3D models would require more detailed information about the boundary

conditions, which are partly unknown. The plug-flow reactor model requires the input of a temperature profile, species concentrations and the overall flowrate of the reactant mixture, the reactor dimensions, pressure, inlet gas viscosity, and an estimation of the normalized internal and external surface area for the implementation of surface reactions and heat transfer. Surface reactions and heat transfer are ignored as the mechanism described in the next paragraph does not include them and the reactor walls are assumed to be isothermal. The reactor dimensions are simplified by assuming that the complete domain (up to 0.5 m) only consists of the quartz tube with an inner diameter of 70 mm. The pressure was set to 1000 mbar as this is the reactor pressure during synthesis. For the inlet gas viscosity, the value for Ar at the assumed temperature was chosen. The volumetric gas flows in the simulation were the ones described in Section 2, assuming homogeneous mixing. The temperature profile was also fed into the model as reported in Ref. [37]. Based on the OES measurements performed here, the gas temperature profile was slightly corrected upwards and the maximum temperature was set to 3700 K. Deviations from this peak temperature value were only observed for C_2 when CO_2 was added into the Ar/H_2 plasma without C_2H_4 present. Because such deviation was observed for these cases only, we assume it originates from a nonthermal effect leading to highly rotationally excited C_2^*, potentially as a result of carbon atom recombination. Based on the measured temperature profile, the residence time and the species concentrations were simulated. The obtained stable species concentrations in the plasma effluent were found to be insensitive to the assumed peak temperature in the plasma, similar to previous work [26]. For comparison, all simulated species profiles are shown in the Supplementary Material for two different peak temperatures (Figures S5–S14). Simulation results for specific cases were compared to GC/MS measurements described in Section 4.1. Gas sampling for GC/MS analysis was performed by connecting evacuated containers to the gas flow at a fixed position at ~0.8 m HAN. Based on the simulations, the species concentrations have reached a stable state at this point and therefore the measurement results can be directly compared to the simulations.

For simulations, the USC Mech Version II [40] and the nitrogen chemistry part from the GRI-Mech 3 mechanism [41] was used. Reactions driven by plasma chemistry were not accounted for. This assumption can be justified by the fact that the plasma is mostly confined to the resonator and no plasma torch reaching into the effluent is observed. Therefore, from distances of HAN > 12 cm, we do not expect a significant fraction of charged species and the process is mainly thermal. The largest species considered in the mechanism were C_6 and C_7 species, with C_6H_2 and benzene (C_6H_6) being the ones with the highest predicted abundance. The formation of solid material as a carbon sink is neglected in the simulation because models that reliably describe the growth of graphene are not available and challenging to implement [37], and more detailed combustion models do not predict carbon growth for the given conditions. Since the solid carbon yield is below 10 wt.% in our experiments, the effect of this simplification is considered negligible. The reliability of the chemical equilibrium calculations are limited to typical combustion temperatures, because the utilized combustion mechanisms only contain a small number of species and some of the species' properties are estimated.

4. Results

4.1. Numerical simulation results and validation

The left ordinate of Fig. 2 shows the results (mole fractions) from the Chemkin numerical kinetics simulation of Case 1. Only the most abundant species and some intermediate species are shown. The simulation can be separated in three distinguishable regions (from 0 to 0.05 m, 0.05 to 0.1 m, and 0.1 to 0.5 m). These three regions are also observed for the other cases studied (see Supplementary Material Section 1). In the first region (from 0 to 0.05 m), the room-temperature homogeneously-mixed gas heats up to ~3700 K. While reaching this value, the reactant(s) decompose, and several unstable decomposition products (e.g., atomic hydrogen, C_2H, and C) are formed. In all cases except for Case 1, also CO is formed within this region. The second region (0.05 to 0.1 m) represents the plasma zone, in which the gas temperature is assumed to be constant and equal to 3700 K, and the species concentrations are
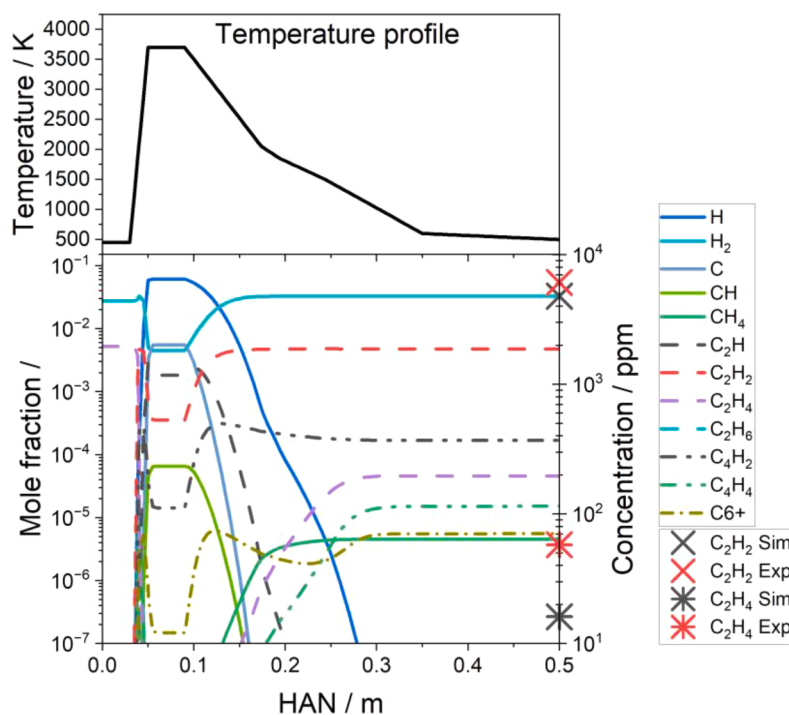
Fig. 2. Temperature profile and kinetics simulation of the species formed in the reactor for Case 1. The comparison between validation measurements by GC/MS and the simulation is shown on the second ordinate on the right (axis uses a different scale).

constant and in thermodynamic equilibrium. The third region (0.1 to 0.5 m) represents the off-gas region in which the gases cool down naturally as they leave the plasma region. Therefore, this region shows a decrease of the temperature down to 600 K, the unstable species disappear, and simple stable molecules are formed (e.g., acetylene/ diacetylene, methane, and ethane). The number of formed hydrocarbons depends on the cooling rate and it is insensitive to the absolute peak temperature. The residence time in the complete simulation domain is calculated to be ~0.9 s with a negligible difference (<10 ms) between the experimental cases. The residence time in the plasma region (HAN = 0.05–0.09 m) is for all cases ~17 ms.

For Cases 1, 4, 7, and 9 (the latter three having a C/O ratio = 2:1.5), the CO, C_2H_2, and C_2H_4 species obtained from the Chemkin simulations were compared to GC/MS measurements. The right *y*-axis of Fig. 2 shows the comparison between experimentally-determined and simulated species concentrations for Case 1. The comparison for all the cases studied is given in Table 2.

Comparing the simulated and measured values for CO, C_2H_2, and C_2H_4 (Table 2 and Fig. 2; right *y*-axis), the C_2H_4 concentrations are underpredicted in the simulations by a factor of 2–3, while the C_2H_2 concentrations do not show a consistent trend of over- or under-prediction (within 20%) by the simulations in respect to the experimental measured values; similar happens to the CO concentrations (within 25%). For Case 7 (with N_2O addition), both the simulation and the measurement show the formation of HCN with similar concentrations to the ones for C_2H_2. However, due to the lack of calibration for the HCN GC signal, its exact value could not be quantified by the GC/MS measurements. The simulated species concentrations strongly depend on the assumed temperature decay rate. The differences in the predicted and assumed C_2H_4 concentrations is unlikely to originate from remaining (i.e., not decomposed) C_2H_4. Previous FTIR measurements [26] with a detection limit of ~1 ppm showed complete decomposition of the reactants at similar conditions (similar microwave power and reactant flowrates). Therefore, the differences between measurement and simulation are attributed to inaccuracies of the temperature profile used as input for the simulations which could affect the formation temperature of C_2H_4 in the plasma off-gas. Non-equilibrium phenomena were observed under certain conditions and the effect of such non-thermal energy distributions on the reaction cannot be excluded. Since the lowest measured temperatures in the plasma zone are already very high, further increase in assumed peak temperatures did not lead to significant changes in the simulation results. The overall process is apparently determined by the conditions in the cooling phase, but not by the peak temperatures. Therefore, it is concluded that the underlying temperature profile decently describes the experimental conditions, because the measured and simulated concentrations for C_2H_2 (and CO) match within 20% (25%). The mass balances for oxygen and carbon are closed by GC/MS measurements of CO, C_2H_2, and C_2H_4 in the reactor off-gas within the measurement uncertainty. These measurements also confirm that the solid carbon yield is below 10%.

Comparing all the simulated cases, Case 1 shows the largest amount of formed C6+ species (i.e., all molecules with six or seven carbon atoms and molar concentrations of >10^{-12}). Upon the addition of any of the employed oxygen carriers, the C6+ concentration decreases by almost two orders of magnitude for C/O ratios of 2:1.5. Fig. 3 shows a comparison for all the oxygen carriers used in the study cases of this work, and the amount of predicted C6+ species. A comparison with H_2O,
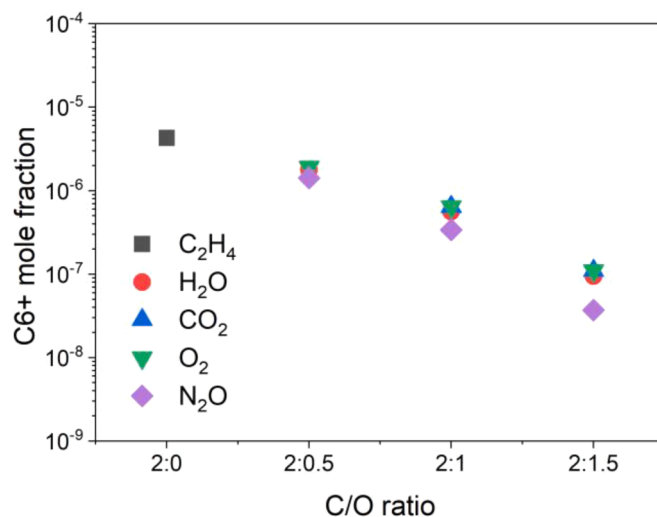
Fig. 3. Mole fractions of C6+ species from kinetics simulations. By the addition of oxygen carriers and lowering the C/O ratio, the mole fraction decreases for all experimental cases almost similarly. As a comparison to a previous publication [26], water is also shown.

which has been used successfully to direct carbon growth previously [26], reveals that all oxygen carriers are expected to act similarly on suppressing the carbon growth. Only the N_2O cases show a stronger reduction because the formation of HCN is predicted, which acts as an additional large gaseous carbon sink together with CO. Water is not formed in relevant concentrations (the simulation yield water concentrations below 10 ppb) because the supplied oxygen is almost completely consumed by CO formation.

An increase in CO concentration is expected with decreasing C/O ratios. The amount of CO produced can herby be interpreted to reduce the amount of available carbon atoms for the growth of solid matter. This has been identified as a good indicator for the growth of graphene and/or soot in previous work [26]. Similarly, a correlation was also observed for the amount of C6+ molecules formed in the simulations. When the amount of produced CO increases, less C6+ species are predicted to form. This is important because C6+ species, such as benzene, are considered to be crucial precursors for carbon growth; thus, having less of them will correlate to less carbon and particle growth.

4.2. Characterization of materials

Fig. 4 shows TEM images of powders harvested at the filter downstream of the reactor (more images are shown in Section 2 of the Supplementary Material). When employing C_2H_4 without the addition of oxygen carriers (Case 1), similar to the literature [26,28], the simultaneous formation of multiple different carbon forms is observed. This includes FLG, small (≤25 nm) soot-like particles, and large (≥80 nm) graphitic particles. Upon the addition of oxygen carriers, different effects are observed: The addition of N_2O and O_2, C/O ratios of 2:0.5 (Cases 2 and 5) alters the formed carbon phase by removing most of the graphitic particles and leading to less soot-like particles present; by increasing the ratio to 2:1.5 (Cases 4 and 7), the undesired particle phases obtained in Case 1 are no longer visible. Unlike for the cases with

Table 2
Comparison of measured and simulated concentrations of CO, C_2H_2, and C_2H_4.

Species	Simulation / ppm				Experiment / ppm			
	Case 1	Case 4	Case 7	Case 9	Case 1	Case 4	Case 7	Case 9
CO	0	7803	7773	15,546	~0	~9600	~8500	~15,300
C_2H_2	4794	1239	772	1234	~4263	~1318	~750	~1477
C_2H_4	38	36	34	36	~105	~94	~75	~94
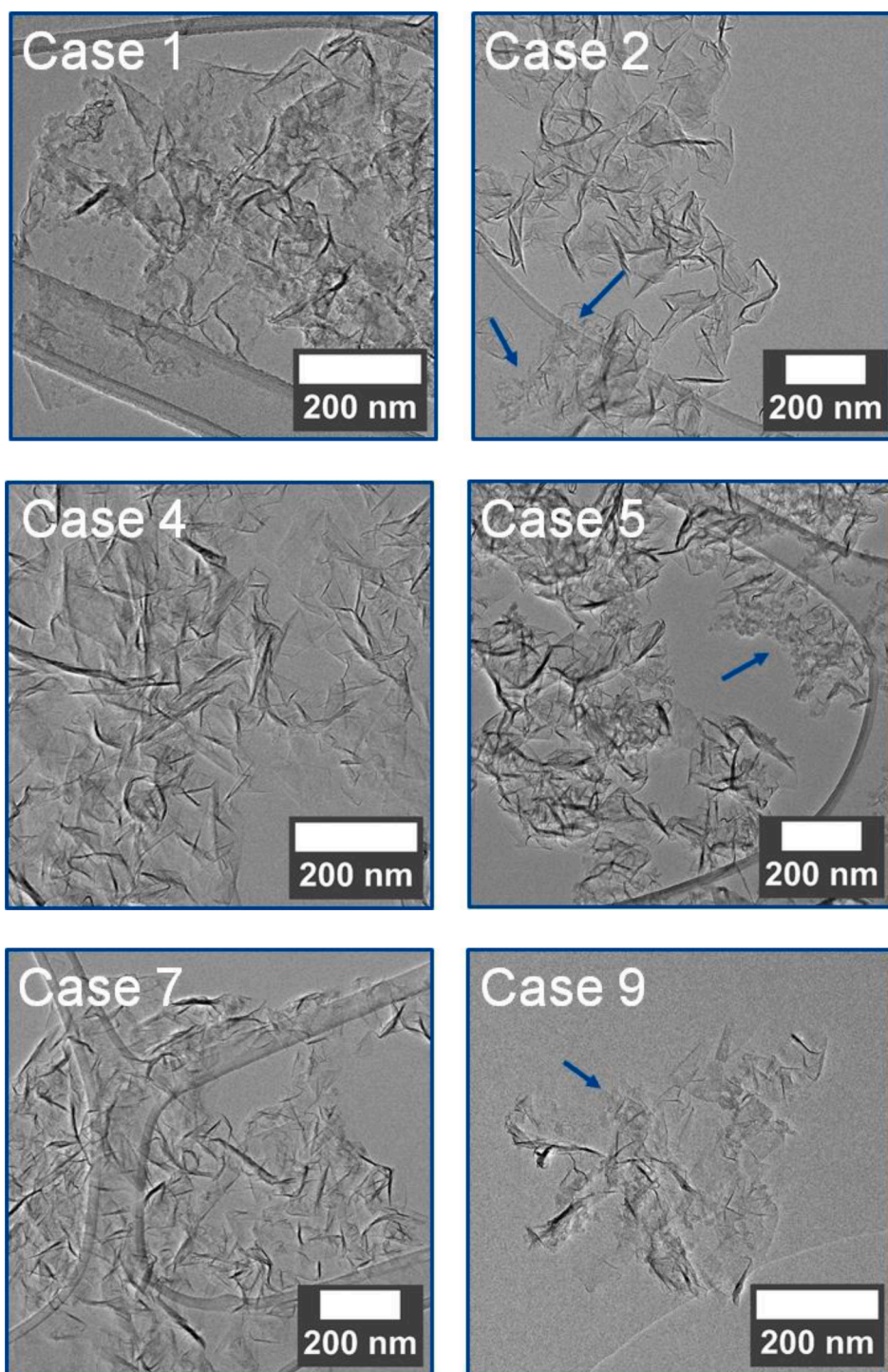
Fig. 4. TEM images of collected and prepared powders. By precursors: pure ethylene (Case 1); addition of O_2 at C/O ratios of 2:0.5 and 2:1.5 (Cases 2 and 4); addition of N_2O at C/O ratios of 2:0.5 and 2:1.5 (Cases 5 and 7); addition of CO_2 at C/O ratio of 2:1.5 (Case 9). Blue arrows indicate example soot-like particles.

N_2O or O_2 addition, the addition of CO_2 (Case 9) does not lead to a complete removal of soot-like particles. In the performed experiments with CO_2 (C/O ratios of 2:1 and 2:1.5; Cases 8 and 9), a sizable number of particles — altogether with FLG — can be found. More images can be found in Figure S16 of the Supplementary Material.

It is also observed that the amount of harvested powder on the downstream filter decreased with the addition of oxygen carrier. The carbon yield for Case 1 (without oxygen carrier) is ~6.6 wt.%, which decreases to 1.1–1.8 wt.% for a C/O ratio of 2:1.5. This global reduction in yield is observed for all oxygen carriers used, including CO_2.

Raman spectroscopy is employed to further probe the microstructural properties of the generated nanocarbon materials. Fig. 5a and b show Raman spectroscopy results for the cases discussed in Fig. 4. For all cases, two spectra were acquired at two different positions on the sample. The second measurements are highlighted by lighter colors. All the individual Raman spectra are shown in detail in Section 3 of the Supplementary Material. The Raman spectra of carbonaceous materials are typically analyzed by fitting and comparing the intensity and width of the different displayed peaks. The most commonly employed peaks to describe the quality of graphene-like materials are D (~1350 cm^{-1}), G
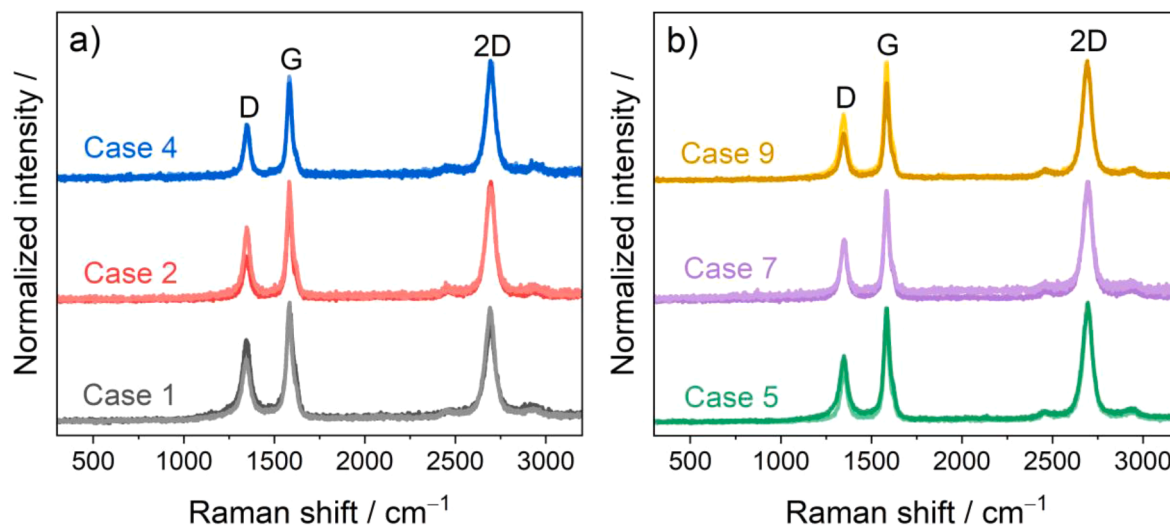
Fig. 5. Raman spectra obtained for the cases in Fig. 4 (range of 300–3200 cm^{-1}). For all cases, two spectra were acquired at two different positions on the sample. The second measurements are highlighted by lighter colors.

($\sim$1580 cm^{-1}), and 2D ($\sim$2700 cm^{-1}). For the analysis of soot-like materials (accounting for amorphous structures), the region around the D and G peaks is typically described by five different components [42].

For Case 1, it is noticeable that the 2D peak appears to be weaker than the G peak and a secondary small shoulder at $\sim$1200 cm^{-1} can be observed. This aligns with the TEM observations, because the shoulder indicates the presence of amorphous carbonaceous particles and a weaker 2D signal can be a sign of significantly less (soot-like particles) and more graphitic material (graphite particles). It can also be observed for Cases 5 and 2. For Cases 4 and 7, however, the relative 2D peak intensity is increased while the shoulder of the D peak disappears. This may be associated to few-layer graphene samples with less impurities. Because the 2D peak can be described with a single Lorentzian line shape, a FWHM of $\sim$55 cm^{-1}, and the A$_{2D/G}$ ratio $>$1.8, we assume a turbostratic stacking order for these samples [43]. Further HRTEM measurements to confirm the few-layer character of prepared samples, are shown in Section 2 of the Supplement for all cases with C/O ratios of 2:1.5.

Case 9 shows a similar behaviour than Cases 4 and 7, yet particles can be clearly observed under the TEM. The difference between the TEM observation and the measured Raman spectra is probably caused by both the relatively small fraction of particles present in the sample but also the difficulty to properly measure and assess the materials properties, because only a small fraction of the collected powders is measured. More than once, the measured Raman spectra of multiple samples containing mixed allotropes changed significantly if another measurement position was chosen, leading to different assessment of the corresponding samples, i.e., pure few-layer graphene or mixture of allotropes. Furthermore, the reported specific weak overtone bands in the range of 1700–2150 cm^{-1} which show distinct differences between different types of graphene-like materials (stacking order and layer number) [44–46], are not observed consistently. Hence, different measurement techniques are necessary and employed.

To estimate the amount of different carbon allotropes present in the samples, thermogravimetric analysis (TGA) was performed given its power to distinguish between different microstructures in carbonaceous samples (soot microstructure [47–49], graphene 'types' [50,51] and their size [52]). TGA can also be used for purification of CNTs [53] or to determine the presence of contaminants [54]. Based on the TGA results, differential thermogravimetric profiles (DTG) were examined, and the signal shape was assigned to different carbonaceous species. The fitted integrated areas of the DTG peaks are used to quantify the respective weight fraction. For the cases in which the peaks could not be

distinguished, the CO$_2$ QMS data (m/z = 44) is used and compared to known mixtures of nanopowders with specific soot-like particle/FLG content to generate reference signals (Section 4 in the Supplementary Material). Similar to the DTG plots, the CO$_2$ QMS measurements contain multiple peaks which can be assigned to the different carbon allotropes. The measurements of the experimental cases are then qualitatively compared to the generated reference signals to estimate a value for the fraction of soot-like particles. Fig. 6 shows the TGA and DTG profiles for Cases 1, 5, 6, and 7. They are chosen to showcase the differences when increasing oxygen-carrier concentrations.

For Case 1 in Fig. 6, several different peaks can be identified. At low temperatures (ca. 650 °C), a peak can be assigned to the presence of soot-like particles in the sample. The main peak at $\sim$730 °C is assigned to few-layer graphene flakes. Both temperature values match well with the ranges reported in literature for soot and FLG oxidation [48,50]. Even a third peak – which was not fitted – can be seen at larger temperatures ($\sim$790 °C), which can be assigned to the generated graphitic particles. To prove that the lowest temperature peak indeed relates to the soot-like particles, control experiments were performed. To generate a reference of soot-like particles, toluene was chosen as reactant as it has already been reported to generate soot-like particles with similar reactant flowrates (refer to previous work [37,55]). The soot-like particle were then measured and samples for Case 1 were oxidized at 660 °C, i.e., heating it up enough to selectively remove the carbon allotrope that is susceptive to oxidation at low temperature. Both approaches confirm that the low temperature peak refers to soot-like particles (find more detail in Section 4 of the Supplementary Material).

For all cases in which the amount of oxygen carrier is increased (see the comparison of Cases 5–7 in Fig. 6), the peak corresponding to the soot-like particles is reduced to the point at which it cannot be observed anymore. Yet, the measured CO$_2$ QMS signal (shown in Fig. S20) at m/z = 44, originating from carbon oxidation, reveals that the samples still contain soot-like particles at C/O ratios of 2:1, i.e., the CO$_2$ signal still shows multiple peaks, while for 2:1.5 they are not distinguishable anymore. Only when CO$_2$ is used as oxygen carrier (Case 9, C/O ratio = 2:1.5), a low oxidising carbon phase can be observed by the QMS data, which is in line with the TEM observation of soot-like particles being present. The estimated content, by fits and qualitative comparison, for the different carbon phases is summarized in Table 3.

Together with the observation by TEM, a carbon content of soot-like particle of 0 wt.% for Case 4 and Case 7 is assumed.

XPS is used to analyze the surface chemistry of the samples. Because both oxygen- and nitrogen-containing reactants are added into the
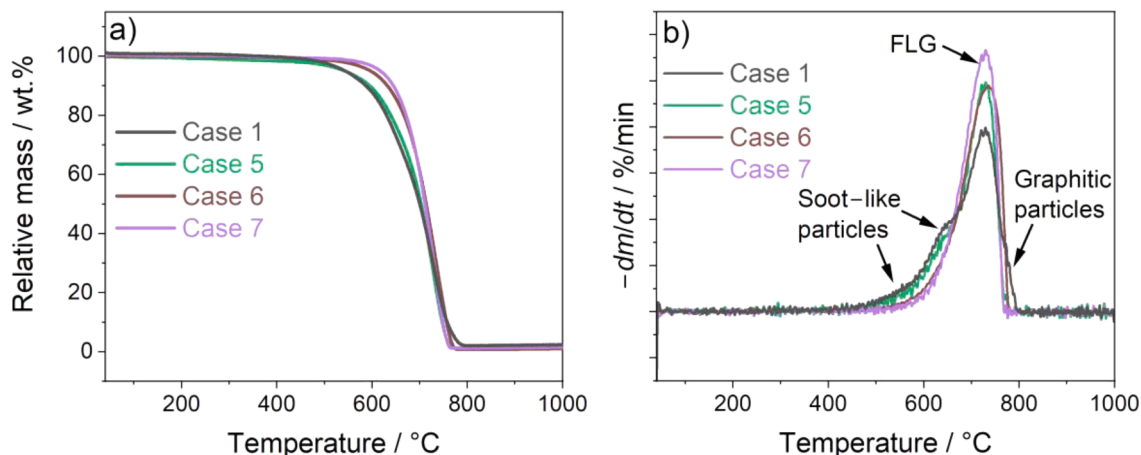
Fig. 6. (a) TGA and b) DTG plots obtained for materials from Cases 1, 5, 6, and 7. Measurements are performed in Ar diluted synthetic air (~15% O_2), with a heating rate of 5 K/min.

Table 3
Content of soot-like particles in wt.% determined by thermogravimetric measurements.

Experiment	Soot particle fraction / wt.%	FLG fraction / wt.%
Case 1	~25	~75
Case 2	~5–10	~90–95
Case 3	<5	>95
Case 4	~0	~100
Case 5	~13	~87
Case 6	~5	~95
Case 7	~0	~100
Case 8	~5	~95
Case 9	<5	>95

reactor, it could occur that part of these atoms end up bonded to the carbon lattice and do not contribute to reactions taking place purely in the gas-phase. Fig. 7 shows the XPS for Case 1 and the cases prepared with the addition of C/O ratios 2:1.5.

All samples have a high purity, i.e., carbon contents of ≥99 at.% as determined by integrating the atomic lines of the survey scan. Comparing the oxygen content, there is no observable difference between the different experimental cases. In all cases, the oxygen content

is below 1 at.% and the slight differences are not considered significant. Furthermore, no nitrogen-bonding to carbon is detected. Therefore, effects or influences by doping or unaccounted heterogeneous reactions between the solid carbon and gaseous atomic species of nitrogen and oxygen can be neglected. One aspect that needs to be mentioned is that the XPS uses a similar measurement spot size as the Raman microscope. Therefore, these measurements have similar drawbacks and e.g., the independent determination of soot/FLG ratio by analyzing, e.g., the C_{1s} high-resolution spectrum becomes challenging (see Section 5 of the Supplementary Material). Still, fitting the high-resolution region of the C_{1s} spectra shows changes in the relative ratio of soot-like particles to FLG in which the soot-like particle fraction was removed at C/O ratios of 2:1.5 for N_2O and O_2 addition (Figure S21).

4.3. Optical emission spectroscopy results

The first step for the spectroscopic investigation of the gas-phase species during plasma synthesis is to analyze the species created upon the admixture of the different oxygen carriers. The comparison is shown in Fig. 8.

For the pristine Ar/H_2 plasma in Fig. 8, only neutral argon (690–840 nm) and hydrogen lines (656 and 486 nm) are visible [56]. When adding
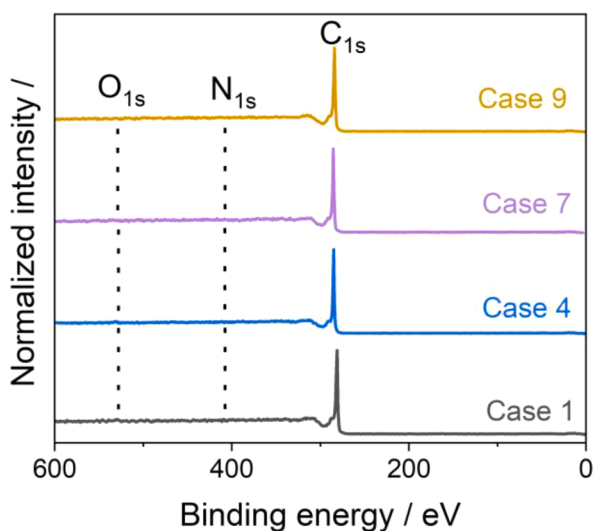
Fig. 7. XPS measurements taken from samples prepared with C/O ratios of 2:1.5 (O_2: Case 4, N_2O: Case 7, CO_2: Case 9) and the reference Case 1.
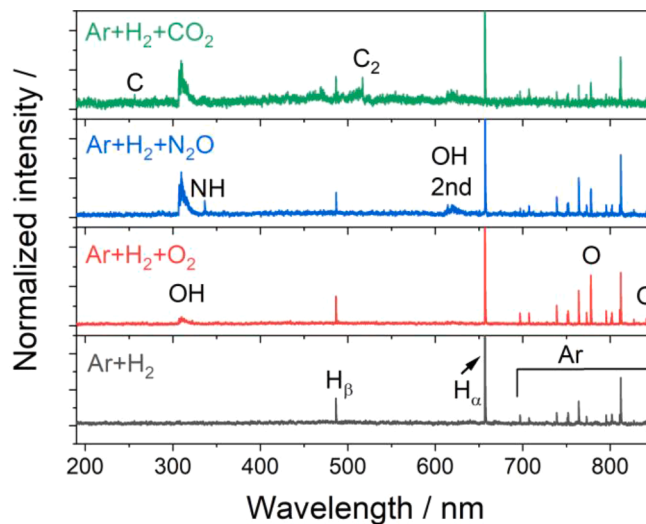
Fig. 8. OES measurements of the plasma. Compared is the pristine argon and hydrogen plasma to the admixture of the different used oxygen carriers. The displayed spectra correspond to Case 4 (O_2), Case 7 (N_2O), and Case 8 (CO_2).

O$_2$ (Case 4), OH lines at ~305 nm [57] and O triplets at ~777 and ~844 nm [56,58] become visible. Both OH and O were also observed when introducing N$_2$O and CO$_2$ into the plasma (Cases 7 and 8, respectively). For N$_2$O (Case 7), NH emission at ~335 nm can also be seen. While the appearance of OH implies its formation by atomic oxygen and hydrogen, the presence of NH indicates the dissociation of N$_2$ formed during N$_2$O decomposition. The presence of NH has been reported in some similar processes, in which N$_2$ was present due to air contamination [59,60]. The observation of O, H, OH, and NH qualitatively agrees with the chemical equilibrium calculations (Figures S2–3), which also predict the presence of these species. CO$_2$ addition leads to C$_2$ Swan band emission at ~516 nm and atomic carbon emission at ~250 nm [56]. Similar observations for CO$_2$ electrical discharges have been reported, as discussed by Carbone et al. [61,62] or by Miotk et al. [63], and it is typically observed for microwave plasma above ~100 mbar. Based on chemical equilibrium calculations, the simultaneous presence of O, OH, and C would be expected to occur for CO$_2$ at temperatures above the assumed plasma temperature of 3700 K only. However, in the plasma non-thermal effects resulting, for example from collisions with metastable Ar might explain the presence of C from CO decomposition already at lower temperatures. Additionally, the line-of-sight light collection of our optical measurements needs to be considered and thus, the species signals can origin from different volume elements in axial direction. When using plasma torch systems or flames, such as in the work by Snirer et al. [64] and Diao et al. [65], spatially-resolved measurements showed a strong spatial dependence of the species distributions close to the nozzle.

The addition of ethylene into the reactor leads for most of the investigated cases to the occurrence of the lines indicated in the lower spectrum of Fig. 9 related to various carbon species.

One can identify Ar and H lines and additional emission of the C$_2$ Swan system. For the region between 190 and 450 nm, the presence of CH [66] and C$_3$ [67] can be confirmed. One of the CH lines might overlap with the C$_2$ Deslandres-d'Azambuja system at ~385 nm [68]. Similar to previous work, lines corresponding to oxygen carriers (O, OH) vanish. In all cases of employing N$_2$O (Case 5–7), strong CN violet band emission at ~380 nm [69] is visible, confirming the intermediate presence of atomic nitrogen.

The detected C$_2$ and OH (prior to C$_2$H$_4$ injection) emission lines are used to calculate rotational temperatures in the plasma region. Because the plasma process is operated at atmospheric pressure, thermal equilibration is assumed and the values for the rotational temperatures are assumed to be equal to the gas temperature. For C$_2$ both the Boltzmann

plot method for lines between 510 and 520 nm and fitting the full spectrum with PGOPHER [70] in the range of 480–520 nm, are employed. The OH emission is analyzed by the Boltzmann plot method only. For most of the experimental cases, the OH and C$_2$ derived temperatures agreed well and temperatures between ~3200–3900 K were measured similar to values estimated in previous works. A comparison of all obtained rotational temperatures is shown in Figure S22 of the Supplementary Material. The only exception is observed for the OH and C$_2$ emission in cases in which CO$_2$ was added without C$_2$H$_4$ (Fig. 8). For, e.g., Case 8, the OH temperature is approx. 3570 K while the C$_2$ derived temperature is ~6100 K (both are calculated with the Boltzmann plot method). Typically, temperatures of >4000 K are required to thermally dissociate CO into atomic carbon and oxygen (CO$_2$ is usually not regarded as a direct source for atomic carbon), so such high rotational temperatures for C$_2$ are not necessarily surprising. The formation of its excited state (d$^3\Pi_g$) can proceed by multiple ways including reactions of two ground state (^{3}P$_J$) carbon atoms with a third body [61] at time scale within ~2 μs which are required to reach thermal equilibrium [71]. However, because such high temperatures are only uniquely observed for the addition of CO$_2$ prior to the injection of C$_2$H$_4$, its presence is more likely a result of non-equilibrium processes.

4.4. Thermophoretic sampling

Thermophoretic sampling of synthesized nanomaterials close to the plasma region was performed to judge whether the distinct morphology differences observed from the *ex situ* filter harvested materials are already present, following the first particle inception and growth zone. That is because earlier investigations showed that FLG morphologically transforms along the axis in the plasma effluent [37]. Case 1 has been investigated as a reference, along with all the oxygen carriers with 2:1.5 C/O ratios. Fig. 10 shows TEM images of the materials collected, displaying abundant small particles on the lacey carbon film. These particles are made out of iron, and they are generated by partial evaporation of the sheath protecting the TEM grid during sampling at low HAN and does not refer the observed soot-like particles.

No distinct differences between the images obtained by *ex situ* analyzed powders for the grown carbon allotropes and the materials collected inside the reactor are observed (as shown in Fig. 4). For the reference Case 1, the sample consists of a mixture of three different carbon allotropes including soot-like particles, graphene flakes, and graphitic particle-like structures. For Case 4 (O$_2$) and Case 7 (N$_2$O), only FLG sheets are observed as the formed product. For Case 9 (CO$_2$), the
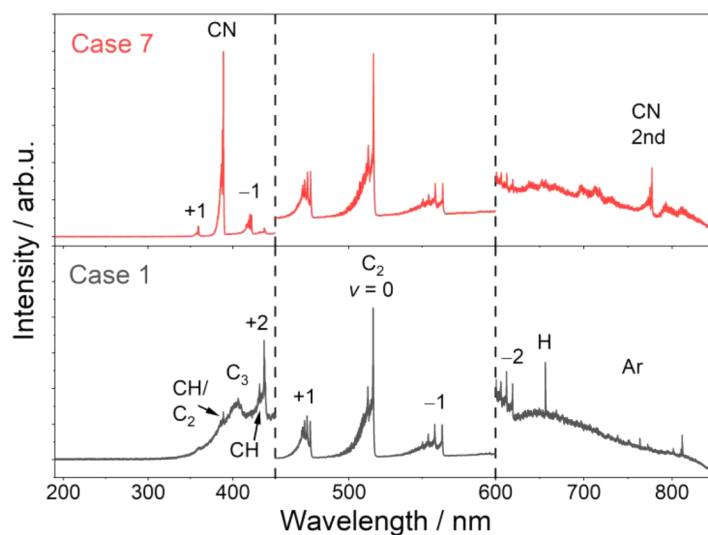
Fig. 9. Emission spectra obtained for Case 1 (pure C$_2$H$_4$) and Case 7 (2:1.5 N$_2$O) after the addition of C$_2$H$_4$. For visibility reasons, both spectra are separated in three different regions. Intensities are on different scales.
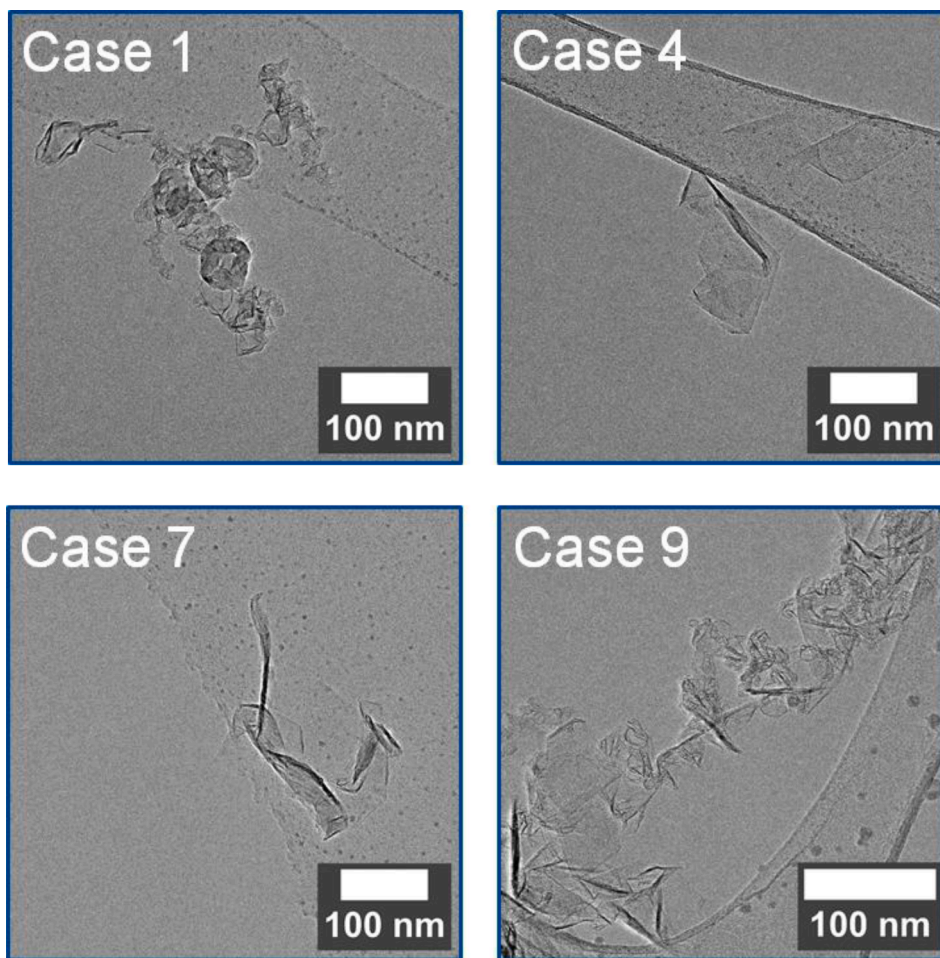
Fig. 10. TEM images of thermophoretically sampled materials. Samples were collected on TEM grids at distance of ~15 cm HAN.

presence of both FLG and soot-like particles is observed.

5. Discussion

The Chemkin simulations indicate a reduction C6+ species upon the addition of the three different oxygen carriers but a negligible difference in between the effect of the oxygen carriers. Based on this result, no significant difference in the formation of the carbon allotropes would be expected for the three oxygen carriers. Based on the simulations, the addition of O_2, N_2O, and CO_2 should – similarly to H_2O – suppress the growth of soot-like particles and favor the formation of FLG with decreasing C/O ratio when added to ethylene. The concentrations obtained from the simulation were compared to the experimental cases with a C/O ratio of 2:1.5 with GC/MS measurements, obtaining a maximum difference of 25% for C_2H_2 and CO. C_2H_4 concentrations were underpredicted by a factor of 2–3, but only represent a small fraction (<1%) of the overall carbon species present in the reactor. Following this expectation, for the cases with O_2 and N_2O addition, an increase in the relative FLG fraction up to the purely FLG was observed when the C/O ratio was decreased from 2:0.5 to 2:1.5. The simultaneous depletion of hydrogen and carbon through the formation of HCN did not show a noticeable effect on the nanocarbon allotropes for the experimental cases with N_2O addition. For cases with CO_2 addition, however, the experiments showed a different behavior. For both Cases 8 and 9, the formation of a small fraction of soot-like particles was noticed, although the yield of solid particles was reduced to levels similar to the cases for O_2 and N_2O.

The TEM results of thermophoretically sampled materials from the near-plasma region (following the first particle inception) and the ones harvested from the filter downstream of the reactor reveal the same carbon allotrope composition. Thus, the distinct allotrope differences are already defined early in the growth process.

To evaluate these observations, OES in the plasma region was performed. It was observed that the species formed differ for the three oxygen carriers. O_2 and N_2O mostly lead to the formation of atomic oxygen or OH. For N_2O, also NH emission is observed. CO_2 apparently does not only lead to the formation of O and OH, but also initiates the formation of C and C_2, where the latter is considered an important growth species for carbon nanomaterials. Rotational temperatures were at ~3570 K for OH for all cases, while the C_2 temperatures reached values up to 6100 K in case of CO_2 added to the plasma in absence of C_2H_2. We attribute this finding to non-thermal effects generating hot electronically excited C_2^*. We nevertheless analyzed the potential effect of such high peak temperatures on the simulations and found that the kinetics simulations are insensitive to such variations in peak temperature and the concentration of the species formed mostly depends on the cooling rate. A comparison between simulations for all cases with two different peak temperatures is given in Section 1 of the Supplementary Material. For both temperature profiles, similar species concentrations are predicted downstream that are comparable to the measured values.

The combination of these results implies that the formation of soot-like particles when CO_2 is used as oxygen carrier is related to the local release/formation of carbon species upon its decomposition because the morphologies are already defined in an early stage downstream of the plasma, as observed by thermophoretic sampling, and the amount of the most abundant hydrocarbon species and carbon monoxide match the

expectations. Their presence might influence the nucleation behavior during the start of carbon formation.

6. Conclusions

Experiments were carried out to investigate the influence of different oxygen carriers on their affinity to suppress the growth of soot-like particles in the plasma pyrolysis of ethylene. Comparing the three oxygen carriers investigated, their addition did lead to a suppression of overall solid carbon growth. For nitrous oxide and molecular oxygen, decreasing C/O ratios led to products enriched in few-layer graphene (FLG). At a C/O ratio of 2:1.5, full suppression for the formation of soot-like particles was observed and pure FLG was obtained. Carbon dioxide addition also led to increased FLG ratios (in comparison to only using ethylene), but a full suppression of soot-like particle growth was not observed. Thermophoretic sampling in the plasma effluent showed that this difference in particle composition was already present in the near-plasma region after the first inception of particles. Optical emission spectroscopy suggests that this might be caused by an additional release of atomic carbon generated by carbon dioxide decomposition. These additional carbon species might be sufficient to influence the nucleation behavior of the first formed carbon nanoparticles.

Appendix A: Supplementary Material

Supplementary Material is available online.

Declaration of Competing Interest

The authors declare that they have no known competing financial interests or personal relationships that could have appeared to influence the work reported in this paper.

Data availability

Data will be made available on request.

Acknowledgment

Supplementary materials

Supplementary material associated with this article can be found, in the online version, at doi:10.1016/j.jaecs.2023.100180.

References

[1] Ferrari AC, Bonaccorso F, Fal`ko V, Novoselov KS, Roche S, Boggild P, et al. Science and technology roadmap for graphene, related two-dimensional crystals, and hybrid systems. Nanoscale 2015;7:4598–810. https://doi.org/10.1039/C4NR01600A.

[2] Šiškins M, Lee M, Wehenkel D, van Rijn R, de Jong TW, Renshof JR, et al. Sensitive capacitive pressure sensors based on graphene membrane arrays. Microsyst Nanoeng 2020;6:102. https://doi.org/10.1038/s41378-020-00212-3.

[3] Choi JH, Lee J, Byeon M, Hong TE, Park H, Lee CY. Graphene-based gas sensors with high sensitivity and minimal sensor-to-sensor variation. ACS Appl Nano Mater 2020;3:2257–65. https://doi.org/10.1021/acsanm.9b02378.

[4] Lee JH, Park SJ, Choi JW. Electrical property of graphene and its application to electrochemical biosensing. Nanomaterials 2019;9:297. https://doi.org/10.3390/nano9020297 (Basel).

[5] Mischke J, Pennings J, Weisenseel E, Kerger P, Rohwerder M, Mertin W, et al. Direct growth of graphene on GaN via plasma-enhanced chemical vapor deposition under N_2 atmosphere. 2D Mater 2020;7:035019. https://doi.org/10.1088/2053-1583/ab8969.

[6] Chamoli P, Das MK, Kar KK. Structural, optical, and electrical characteristics of graphene nanosheets synthesized from microwave-assisted exfoliated graphite. J Appl Phys 2017;122:185105. https://doi.org/10.1063/1.4991577.

[7] Zhang Y, Li H, Kuo L, Dong P, Yan F. Recent applications of graphene in dye-sensitized solar cells. Curr Opin Colloid Interface Sci 2015;20:406–15. https://doi.org/10.1016/j.cocis.2015.11.002.

[8] Yang Z, Yao Z, Li G, Fang G, Nie H, Liu Z, et al. Sulfur-doped graphene as an efficient metal-free cathode catalyst for oxygen reduction. ACS Nano 2012;6:205–11. https://doi.org/10.1021/nn203393d.

[9] Bertin E, Münzer A, Reichenberger S, Streubel R, Vinnay T, Wiggers H, et al. Durability study of platinum nanoparticles supported on gas-phase synthesized graphene in oxygen reduction reaction conditions. Appl Surf Sci 2019;467-468:1181–6. https://doi.org/10.1016/j.apsusc.2018.10.061.

[10] Xiang H, Zhang K, Ji G, Lee JY, Zou C, Chen X, et al. Graphene/nanosized silicon composites for lithium battery anodes with improved cycling stability. Carbon 2011;49:1787–96. https://doi.org/10.1016/j.carbon.2011.01.002. N.Y.

[11] Münzer A, Xiao L, Sehlleier YH, Schulz C, Wiggers H. All gas-phase synthesis of graphene: characterization and its utilization for silicon-based lithium-ion batteries. Electrochim Acta 2018;272:52–9. https://doi.org/10.1016/j.electacta.2018.03.137.

[12] Yang W, Ni M, Ren X, Tian Y, Li N, Su Y, et al. Graphene in supercapacitor applications. Curr Opin Colloid Interface Sci 2015;20:416–28. https://doi.org/10.1016/j.cocis.2015.10.009.

[13] Pope MA, Punckt C, Aksay IA. Intrinsic capacitance and redox activity of functionalized graphene sheets. J Phys Chem C 2011;115:20326–34. https://doi.org/10.1021/jp2068667.

[14] Nakahara K, Knego J, Sloop T, Bisquera C, Subler N, Dato A. Enhanced mechanical properties of epoxy-matrix nanocomposites reinforced with graphene synthesized in atmospheric plasmas. Plasma Process Polym 2020;17:1900244. https://doi.org/10.1002/ppap.201900244.

[15] Kim H, Abdala AA, Macosko CW. Graphene/Polymer Nanocomposites. Macromolecules 2010;43:6515–30. https://doi.org/10.1021/ma100572e.

[16] Song WL, Cao MS, Lu MM, Bi S, Wang CY, Liu J, et al. Flexible graphene/polymer composite films in sandwich structures for effective electromagnetic interference shielding. Carbon 2014;66:67–76. https://doi.org/10.1016/j.carbon.2013.08.043. N.Y.

[17] Diab J, Fulcheri L, Hessel V, Rohani V, Frenklach M. Why turquoise hydrogen will Be a game changer for the energy transition. Int J Hydrog Energy 2022;47:25831–48. https://doi.org/10.1016/j.ijhydene.2022.05.299.

[18] Fulcheri L, Rohani VJ, Wyse E, Hardman N, Dames E. An energy-efficient plasma methane pyrolysis process for high yields of carbon black and hydrogen. Int J Hydrog Energy 2023;48:2920–8. https://doi.org/10.1016/j.ijhydene.2022.10.144.

[19] Zafar MA, Liu Y, Hernandez FCR, Varghese OK, Jacob MV. Plasma-based synthesis of freestanding graphene from a natural resource for sensing application. Adv Mater Interfaces 2023;10:2202399. https://doi.org/10.1002/admi.202202399.

[20] Toman J, Jasek O, Snirer M, Kudrle V, Jurmanova J. On the interplay between plasma discharge instability and formation of free-standing graphene nanosheets in a dual-channel microwave plasma torch at atmospheric pressure. J Phys D Appl Phys 2019;52:265205. https://doi.org/10.1088/1361-6463/ab0f69.

[21] Shavelkina MB, Ivanov PP, Amirov RK, Bocharov AN, Drachev AI, Shavelkin MA. Plasma pyrolysis of ethanol for the production of carbon nanostructures. High Energy Chem 2021;55:531–6. https://doi.org/10.1134/S001814392106014X.

[22] Aissou T, Casteignau F, Braidy N, Veilleux J. Synthesis and growth of onion-like polyhedral graphitic nanocapsules by thermal plasma. Plasma Chem Plasma Process 2023;43:413–27. https://doi.org/10.1007/s11090-023-10314-1.

[23] Bundaleska N, Tsyganov D, Dias A, Felizardo E, Henriques J, Dias FM, et al. Microwave plasma enabled synthesis of free standing carbon nanostructures at atmospheric pressure conditions. Phys Chem Chem Phys 2018;20:13810–24. https://doi.org/10.1039/C8CP01896K.

[24] Dato A, Frenklach M. Substrate-free microwave synthesis of graphene: experimental conditions and hydrocarbon precursors. New J Phys 2010;12:125013. https://doi.org/10.1088/1367-2630/12/12/125013.

[25] Fronczak M, Fazekas P, Károly Z, Hamankiewicz B, Bystrzejewski M. Continuous and catalyst free synthesis of graphene sheets in thermal plasma jet. Chem Eng J 2017;322:385–96. https://doi.org/10.1016/j.cej.2017.04.051.

[26] Fortugno P, Musikhin S, Shi X, Wang H, Wiggers H, Schulz C. Synthesis of freestanding few-layer graphene in microwave plasma: the role of oxygen. Carbon 2022;186:560–73. https://doi.org/10.1016/j.carbon.2021.10.047. N.Y.

[27] Hof F, Kampioti K, Huang K, Jaillet C, Derré A, Poulin P, et al. Conductive inks of graphitic nanoparticles from a sustainable carbon feedstock. Carbon 2017;111:142–9. https://doi.org/10.1016/j.carbon.2016.09.052. N.Y.

[28] Ma J, Chen X, Song M, Wang C, Xia W. Study on formation mechanism of three types of carbon nanoparticles during ethylene pyrolysis in thermal plasmas. Diam Relat Mater 2021;117:108445. https://doi.org/10.1016/j.diamond.2021.108445.

[29] Fronczak M, Keszler AM, Mohai M, Jezsó B, Farkas A, Károly Z. Facile and continuous synthesis of graphene nanoflakes in RF thermal plasma. Carbon 2022;193:51–67. https://doi.org/10.1016/j.carbon.2022.03.008. N.Y.

[30] Chen X, Wang C, Song M, Ma J, Ye T, Xia W. The morphological transformation of carbon materials from nanospheres to graphene nanoflakes by thermal plasma. Carbon 2019;155:521–30. https://doi.org/10.1016/j.carbon.2019.08.077. N Y.

[31] Zhang D, Xie Z, Zhang K, Wang H, Qu T, Ma W, et al. Controlled regulation of the transformation of carbon nanomaterials under H₂ mixture atmosphere by arc plasma. Chem Eng Sci 2021;241:116695. https://doi.org/10.1016/j.ces.2021.116695.

[32] Shavelkina MB, Ivanov PP, Bocharov AN, Amirov RK. Numerical and experimental study of the multichannel nature of the synthesis of carbon nanostructures in DC plasma jets. Plasma Chem Plasma Process 2021;41:171–89. https://doi.org/10.1007/s11090-020-10133-8.

[33] Singh M, Sengupta A, Zeller K, Skoptsov G. Vander Wal RL. effect of hydrogen concentration on graphene synthesis using microwave-driven plasma-mediated methane cracking. Carbon 2019;143:802–13. https://doi.org/10.1016/j.carbon.2018.11.082. N Y.

[34] Jašek O, Toman J, Šnírer M, Jurmanová J, Kudrle V, Michalička J, et al. Microwave plasma-based high temperature dehydrogenation of hydrocarbons and alcohols as a single route to highly efficient gas phase synthesis of freestanding graphene. Nanotechnology 2021;32:505608. https://doi.org/10.1088/1361-6528/ac24c3.

[35] Musikhin S, Fortugno P, Endres T, Dreier T, Daun KJ, Schulz C. Elemental carbon and hydrogen concentrations as the main factors in gas-phase graphene synthesis: quantitative fourier-transform infrared spectroscopy study. Carbon 2023;202:47–60. https://doi.org/10.1016/j.carbon.2022.11.024. N Y.

[36] Kunze F, Kuns S, Spree M, Hülser T, Schulz C, Wiggers H, et al. Synthesis of silicon nanoparticles in a pilot-plant-scale microwave plasma reactor: impact of flow rates and precursor concentration on the nanoparticle size and aggregation. Powder Technol 2019;342:880–6. https://doi.org/10.1016/j.powtec.2018.10.042.

[37] López-Cámara CF, Fortugno P, Asif M, Musikhin S, Prindler C, Wiggers H, et al. Evolution of particle size and morphology in plasma synthesis of few-layer graphene and soot. Combust Flame 2023:112713. https://doi.org/10.1016/j.combustflame.2023.112713.

[38] Suleiman S, Nanjaiah M, Skenderovic I, Rosenberger T, Kunze F, Wlokas I, et al. Atmospheric-pressure particle mass spectrometer for investigating particle growth in spray flames. J Aerosol Sci 2021;158:105827. https://doi.org/10.1016/j.jaerosci.2021.105827.

[39] Lim JM, Swami A, Gilson LM, Chopra S, Choi S, Wu J, et al. Ultra-high throughput synthesis of nanoparticles with homogeneous size distribution using a coaxial turbulent jet mixer. ACS Nano 2014;8:6056–65. https://doi.org/10.1021/nn501371n.

[40] Wang H, You X, Joshi AV, Davis SG, Laskin A, Egolfopoulos F, et al. USC mech version II. High-temperature combustion reaction model of H₂/CO/C1-C4 compounds. ; 2007.https://ignis.usc.edu:80/Mechanisms/USC-Mech%20II/USC_Mech%20II.ht

[41] Smith GP, Golden DM, Frenklach M, Moriarty NW, Eiteneer B, Goldenberg M, et al. GRI-Mech 3(0). http://combustion.berkeley.edu/gri-mech/version30/text30.html.

[42] Sadezky A, Muckenhuber H, Grothe H, Niessner R, Pöschl U. Raman microspectroscopy of soot and related carbonaceous materials: spectral analysis and structural information. Carbon 2005;43:1731–42. https://doi.org/10.1016/j.carbon.2005.02.018. N Y.

[43] Malard LM, Pimenta MA, Dresselhaus G, Dresselhaus MS. Raman spectroscopy in graphene. Phys Rep 2009;473:51–87. https://doi.org/10.1016/j.physrep.2009.02.003.

[44] Cong C, Yu T, Saito R, Dresselhaus GF, Dresselhaus MS. Second-order overtone and combination raman modes of graphene layers in the range of 1690−2150 cm⁻¹. ACS Nano 2011;5:1600–5. https://doi.org/10.1021/nn200010m.

[45] Rao R, Podila R, Tsuchikawa R, Katoch J, Tishler D, Rao AM, et al. Effects of layer stacking on the combination raman modes in graphene. ACS Nano 2011;5:1594–9. https://doi.org/10.1021/nn1031017.

[46] Garlow JA, Barrett LK, Wu L, Kisslinger K, Zhu Y, Pulecio JF. Large-area growth of turbostratic graphene on Ni(111) via physical vapor deposition. Sci Rep 2016;6:19804. https://doi.org/10.1038/srep19804.

[47] Niessner R. The many faces of soot: characterization of soot nanoparticles produced by engines. Angew Chem Int Ed 2014;53:12366–79. https://doi.org/10.1002/anie.201402812.

[48] Hagen F, Hardock F, Koch S, Sebbar N, Bockhorn H, Loukou A, et al. Why soot is not alike soot: a molecular/nanostructural approach to low temperature soot oxidation. Flow Turbul Combust 2021;106:295–329. https://doi.org/10.1007/s10494-020-00205-2.

[49] Kreuznacht S, Purcel M, Böddeker S, Awakowicz P, Xia W, Muhler M, et al. Comparison of the performance of a microwave plasma torch and a gliding arc plasma for hydrogen production via methane pyrolysis. Plasma Processes Polym 2023;20:2200132. https://doi.org/10.1002/ppap.202200132.

[50] Farivar F, Yap PL, Hassan K, Tung TT, Tran DNH, Pollard AJ, et al. Unlocking thermogravimetric analysis (TGA) in the fight against "Fake graphene" materials. Carbon 2021;179:505–13. https://doi.org/10.1016/j.carbon.2021.04.064. N Y.

[51] Jašek O, Toman J, Všianský D, Jurmanová J, Šnírer M, Hemzal D, et al. Controlled high temperature stability of microwave plasma synthesized graphene nanosheets. J Phys D Appl Phys 2021;54:165201. https://doi.org/10.1088/1361-6463/abdb6d.

[52] Farivar F, Lay Yap P, Karunagaran RU, Losic D. Thermogravimetric analysis (TGA) of graphene materials: effect of particle size of graphene, graphene oxide and graphite on thermal parameters. C. 2021;7:41. https://doi.org/10.3390/c7020041.

[53] Picheau E, Hof F, Derré A, Amar S, Noé L, Monthioux M, et al. Burn them right! determining the optimal temperature for the purification of carbon materials by combustion. C. 2022;8:31. https://doi.org/10.3390/c8020031.

[54] Toman J, Šnírer M, Rincón R, Jašek O, Všianský D, Raya AM, et al. On the gas-phase graphene nanosheet synthesis in atmospheric microwave plasma torch: upscaling potential and graphene nanosheet-copper nanocomposite oxidation resistance. Fuel Process Technol 2023;239:107534. https://doi.org/10.1016/j.fuproc.2022.107534.

[55] Musikhin S, Fortugno P, Corbin JC, Smallwood GJ, Dreier T, Daun KJ, et al. Characterization of few-layer graphene aerosols by laser-induced incandescence. Carbon 2020;167:870–80. https://doi.org/10.1016/j.carbon.2020.05.052. N Y.

[56] Kramida A, Rachelko Y, Reader J, Team NA. NIST atomic spectra database (version 5.10). Gaithersburg, MD: National Institute of Standards and Technology; 2022. https://doi.org/10.18434/T4W30F. Available: https://physics.nist.gov/asd.

[57] Dieke GH, Crosswhite HM. The ultraviolet bands of OH fundamental data. J Quant Spectrosc Radiat Transf 1962;2:97–199. https://doi.org/10.1016/0022-4073(62)90061-4.

[58] Milosavljević V, Donegan M, Cullen PJ, Dowling DP. Diagnostics of an O₂–He RF atmospheric plasma discharge by spectral emission. J Phys Soc Jpn 2013;83:014501. https://doi.org/10.7566/JPSJ.83.014501.

[59] Rincón R, Marinas A, Muñoz J, Melero C, Calzada MD. Experimental research on ethanol-chemistry decomposition routes in a microwave plasma torch for hydrogen production. Chem Eng J 2016;284:1117–26. https://doi.org/10.1016/j.cej.2015.09.062.

[60] Melero C, Rincón R, Muñoz J, Zhang G, Sun S, Perez A, et al. Scalable graphene production from ethanol decomposition by microwave argon plasma torch. Plasma Phys Controlled Fusion 2018;60:014009. https://doi.org/10.1088/1361-6587/aa8480.

[61] Carbone E, D'Isa F, Hecimovic A, Fantz U. Analysis of the C₂ Swan bands as a thermometric probe in CO₂ microwave plasmas. Plasma Sources Sci Technol 2020;29:055003. https://doi.org/10.1088/1361-6595/ab74b4.

[62] D'Isa FA, Carbone EAD, Hecimovic A, Fantz U. Performance analysis of a 2.45GHz microwave plasma torch for CO₂ decomposition in gas swirl configuration. Plasma Sources Sci Technol 2020;29:105009. https://doi.org/10.1088/1361-6595/abaa84.

[63] Miotk R, Hrycak B, Czylkowski D, Dors M, Jasinski M, Mizeraczyk J. Liquid fuel reforming using microwave plasma at atmospheric pressure. Plasma Sources Sci Technol 2016;25:035022. https://doi.org/10.1088/0963-0252/25/3/035022.

[64] Snirer M, Kudrle V, Toman J, Jašek O, Jurmanová J. Structure of microwave plasma-torch discharge during graphene synthesis from ethanol. Plasma Sources Sci Technol 2021;30:065020. https://doi.org/10.1088/1361-6595/abfbea.

[65] Diao Z, Winter M, Hirasawa T, Kato Y, Ishino Y, Saito K. Characterization of six clustered methane-air diffusion microflames through spectroscopic and tomographic analysis of CH* and C2* chemiluminescence. Exp Therm Fluid Sci 2019;102:20–7. https://doi.org/10.1016/j.expthermflusci.2018.10.032.

[66] Bleekrode R, Nieuwpoort WC. Absorption and emission measurements of C₂ and CH electronic bands in low-pressure oxyacetylene flames. J Chem Phys 1965;43:3680–7. https://doi.org/10.1063/1.1696536.

[67] Oliver J, Bharadwaj N, Sizyuk T. Laser-induced fluorescence of C₂ and C₃ in colliding carbon plasma. J Appl Phys 2019;125:073301. https://doi.org/10.1063/1.5078641.

[68] Acquaviva S, Giorgi MLD. High-resolution investigations of C₂ and CN optical emissions in laser-induced plasmas during graphite ablation. J Phys B 2002;35:795. https://doi.org/10.1088/0953-4075/35/4/304. Atomic, Molecular and Optical Physics.

[69] Brooke JSA, Ram RS, Western CM, Li G, Schwenke DW, Bernath PF. Einstein A coefficients and oscillator stenghts for the A²Π–X²Σ⁺ (red) and B²Σ⁺–X²Σ⁺ (violet) systems and rovibrational transitions in the X²Σ⁺ state of CN. Astrophys J Suppl Ser 2014;210:23. https://doi.org/10.1088/0067-0049/210/2/23.

[70] Western CM. PGOPHER: a program for simulating rotational, vibrational and electronic spectra. J Quant Spectrosc Radiat Transfer 2017;186:221–42. https://doi.org/10.1016/j.jqsrt.2016.04.010.

[71] Soldatov S, Link G, Silberer L, Schmedt CM, Carbone E, D'Isa F, et al. Time-resolved optical emission spectroscopy reveals nonequilibrium conditions for CO₂ splitting in atmospheric plasma sustained with ultrafast microwave pulsation. ACS Energy Lett 2021;6:124–30. https://doi.org/10.1021/acsenergylett.0c01983.